Persistent Large Anisotropic Magnetoresistance and Insulator-to-Metal Transition in Spin-Orbit-Coupled $Sr_2(Ir_{1-x}Ga_x)O_4$ for Antiferromagnetic Spintronics

Haowen Wang,[1] Wei Wang,[1] Ni Hu,[2] Tianci Duan,[2] Songliu Yuan,[1] Shuai Dong,[3] Chengliang Lu,[1,*] and Jun-Ming Liu[4,5]

[1]*School of Physics & Wuhan National High Magnetic Field Center, Huazhong University of Science and Technology, Wuhan 430074, China*

[2]*School of Science and Hubei Collaborative Innovation Center for High-Efficiency Utilization of Solar Energy, Hubei University of Technology, Wuhan 430068, China*

[3]*School of Physics, Southeast University, Nanjing 211189, China*

[4]*Laboratory of Solid State Microstructures and Innovation Center of Advanced Microstructures, Nanjing University, Nanjing 210093, China*

[5]*Institute for Advanced Materials, Hubei Normal University, Huangshi 435001, China*

(Received 23 January 2018; revised manuscript received 24 April 2018; published 25 July 2018)

Antiferromagnetic (AFM) spintronics, where magnetotransport is governed by an antiferromagnet instead of a ferromagnet, opens fascinating new perspectives for both fundamental research and device technology. This is because AFM spintronics have intrinsic appealing properties, such as rigidness to magnetic field, absence of stray field, and ultrafast spin dynamics. One of the urgent challenges, hindering the realization of the full potential of AFM spintronics, is the performance gap between AFM metals and insulators. Here, we demonstrate the insulator-metal transition and persistently large anisotropic magnetoresistance (AMR) in single crystals $Sr_2(Ir_{1-x}Ga_x)O_4$ ($0 \le x \le 0.09$), which host the same basal-plane AFM lattice with strong spin-orbit coupling. The nondoped Sr_2IrO_4 shows the insulating transport with AMR as large as approximately 16.8% at 50 K. The Ga substitution of Ir allows a gradual reduction of electrical resistivity. A clear insulator-to-metal transition is identified in doped samples with x above 0.05, while the AMR can still have approximately 1%, which is sizable in comparison with those in the AFM metals reported so far. Our experiments reveal that all samples have similar fourfold AMR symmetry, which can be well understood in the scenario of magnetocrystalline anisotropy. It is suggested that the spin-orbit-coupled antiferromagnets $Sr_2(Ir_{1-x}Ga_x)O_4$ are promising candidate materials for AFM spintronics, providing a rare opportunity to integrate the superior spintronic functionalities of AFM metals and insulators.

DOI: 10.1103/PhysRevApplied.10.014025

I. INTRODUCTION

Antiferromagnets have generated increased interest in the spintronics community, owing to their attractive properties and their technological potential to develop efficient memory devices [1–8]. The appealing features, such as rigidity to external magnetic field, absence of stray field, and ultrafast spin dynamics, make the antiferromagnetic (AFM) materials particularly favorable for ultrahigh density and high-speed spintronics [7]. A major breakthrough in this emerging AFM spintronics field is the observation of anisotropic magnetoresistance (AMR) in several antiferromagnets recently [1,3,4,6,8,9], which confirmed the viability of utilizing antiferromagnets in spintronic devices [10]. When the staggered spin orders in antiferromagnets are manipulated by various approaches, the equilibrium relativistic electronic structure is expected to be modified. As a consequence, the AFM orders can be electrically readout by the AMR effect, which is the magnetotransport counterpart of the relativistic energy anisotropy.

Studies of AFM-based AMR (AFM AMR) have illustrated the leading role of strong spin-orbit coupling (SOC) in the manipulation and detection of AFM orders well. This has stimulated the search for new materials combining Néel orders and the strong SOC effect. A straightforward and efficient method using strong SOC is to alloy 3*d* magnetic species with heavier elements. For instance, a spin-valve-like magnetoresistance (MR), as large as 160%, was observed in a MnIr-based tunneling junction [1], and room temperature (T) memory was revealed in a simple resistor made of AFM FeRh [4]. Recently, the discovery of

*cllu@mail.hust.edu.cn

 © 2018 American Physical Society

a $J_{\text{eff}} = 1/2$ state in several $5d$ iridates has posed a fundamentally distinct scheme to build up a spin-orbit-coupled AFM lattice, where the SOC and magnetic moment have the same source, i.e., the Ir ions [11–15]. In fact, cases of large SOC involved in building up the electronic and magnetic structures have been widely seen in $4d/5d$ magnetic materials [16,17]. Because of the pronounced SOC (scaled by a factor $\lambda \sim 0.5$ eV) at the Ir site in iridates, the t_{2g} band of the Ir $5d$ state is split into half-filled $J_{\text{eff}} = 1/2$ and fully occupied $J_{\text{eff}} = 3/2$ bands. Further, the $J_{\text{eff}} = 1/2$ band can be split by a moderate Hubbard repulsion, leading to a Mott transition [11]. Interestingly, the $J_{\text{eff}} = 1/2$ moment, entangling both spin and orbital momenta, was found to be a very efficient ingredient for AFM spintronics. In the prototypical $J_{\text{eff}} = 1/2$ AFM insulator Sr_2IrO_4, giant relativistic energy anisotropy was predicted upon the AFM spin-axis rotation [3], and a remarkable AMR of approximately 14% was experimentally evidenced [5]. Although fascinating functionalities have been identified in the AFM metallic alloys and insulating oxides separately, it remains a significant challenge to integrate these superior properties properly, which hinders the realization of the full potential of AFM spintronics. For instance, the AFM metals are suitable for electrical writing of information, while the AFM insulators are more compatible with transistors.

Difficulties for closing the performance gap between AFM metals and insulators lie mostly in finding appropriate materials in which the electric transport can be tuned over a broad range, i.e., from metallic to insulating, without breaking the inherent AFM lattice and especially the related spintronic functionalities, e.g., the AMR effect. This has actually been one of the main obstacles to the advancement of AFM spintronics. In comparison with AFM alloys showing robust metallicity, the $J_{\text{eff}} = 1/2$ Mott state in iridates, i.e., in Sr_2IrO_4, is found to be rather tunable, such as the insulator-metal transition induced by doping [18–21]. In particular, hidden orders like pseudogap and Fermi arcs were experimentally identified in doped Sr_2IrO_4, in analogy to those found in the high-temperature cuprate superconductors [22–24].

To realize an AFM AMR effect in Sr_2IrO_4 and its derivate, a robust AFM lattice is strongly desired and has to be maintained in the doping-induced metallic state. So far, the AFM AMR has already been identified in the nondoped Sr_2IrO_4, which was understood as a consequence of magnetocrystalline anisotropy [3,5]. However, previous works focusing on the insulator-metal transition in doped Sr_2IrO_4 have commonly found that the basal-plane AFM lattice is prone to collapse upon the presence of metallic state [18–21]. This is intriguing indeed, since a signature character of Sr_2IrO_4 is the absence of anomaly in the electric transport corresponding to the AFM transition at $T_N \sim 240$ K [19]. In fact, several recent theoretical calculations predicted the coexistence of AFM order with metallic state in Sr_2IrO_4 upon pure carrier doping [25–27]. To achieve this, nonmagnetic species doping, which can exclude possible additional magnetic perturbations being brought into the system, should be preferential. In addition, substituting Ir with nonmagnetic ions in Sr_2IrO_4 may further enhance the local Ir(Ga)-p/O-d hybridization and thereby the structure distortion, which usually favors the AFM interaction. Indeed, Liu *et al*. theoretically revealed a vital role of the p-d hybridization in tuning structure distortion in doped Sr_2IrO_4 [28]. Therefore, doping the $J_{\text{eff}} = 1/2$ Mott state with nonmagnetic species in Sr_2IrO_4, in comparison with those magnetic doping, provides a promising route to solve the urgent issue of the apparent incompatibility of robust AFM order with metallic transport.

In the present work, we demonstrate successive modulation of the electric transport from insulating state to metallic state in nonmagnetic Ga-doped Sr_2IrO_4 single crystals, while the robust AFM orders and persistently large crystalline AMR can be retained. For Sr_2IrO_4, the AMR is found to be as big as approximately 16.8% at $T = 50$ K, while the doped samples show not only metallic transport but also AMR larger than approximately 1%. All samples show the same fourfold AMR symmetry, arising from the magnetocrystalline anisotropy.

II. EXPERIMENTS

$Sr_2(Ir_{1-x}Ga_x)O_4$ $(0 \leq x \leq 0.09)$ single crystals are synthesized from off-stoichiometric quantities of $SrCl_2$, Sr_2CO_3, IrO_2, and Ga_2O_3 using self-flux techniques. In order to determine the crystalline structure, select crystals are crashed thoroughly and then powder XRD measurements are performed at room temperature. The ionic oxidation state of Ir is determined by performing x-ray photoelectron spectroscopy (XPS) measurements. Atomic force microscopy characterizations are performed to capture the surface morphology of the crystals after cleaving.

Electric transport measurements for all samples are carried out using a four-probe method in a Quantum Design (QD) physical property measurement system equipped with a rotator module. With regard to the AMR measurements, exciting current I is applied along the [001] direction, and the magnetic field H is always rotated within the basal plane of the crystals. Therefore, AMR refers to the (I, H) behaviors. Magnetization (M) as a function of T and H is measured using a QD superconducting quantum-interference device. During the $M(T)$ measurements in both the in-plane and out-of-plane geometries, the measuring field is fixed at $H = 0.1$ T. All $M(H)$ curves are measured after the zero-field-cooled (ZFC) sequence.

III. RESULTS

All samples with different Ga-doping content x show the pure phase with a tetragonal crystalline structure, evidenced by the measured XRD patterns presented in Fig.

S1 of the Supplemental Material [29]. To check the crystal quality, the sample with $x = 0.07$ is cleaved, and then the surface morphology is mapped out through atomic force microscopy characterization, from which the layered structure can be clearly seen (see Fig. S2 of the Supplemental Material [29]). To obtain more details on the structure variation upon Ga doping, Rietveld-profile refining of the XRD data is performed, and the refined details for the sample with $x = 0.05$ are presented in Fig. 1. The difference between the measured and refined spectra is small with reliability parameter $R_{wp} = 6.78\%$. For all other samples, R_{wp} values are at similar levels. The lattice parameters, including a and c values, and Ir-O-Ir bending angle φ and IrO_6 octahedron rotation angle ϕ [$= (180° - \varphi)/2$] are shown in Figs. 1(b) and 1(c), respectively. Both a and c values just show a tiny variation upon doping, as small as approximately 0.1% and approximately −0.2%, respectively, over the x range from 0.0 to 0.09. This behavior is expected because of the approximate ionic radius of Ga^{3+} (0.620 Å) and Ir^{4+} (0.625 Å) [30]. In contrast, both φ and ϕ values show non-negligible variations upon Ga doping, e.g., φ is enhanced by approximately 4° while ϕ is reduced by approximately 2° as x is up to 0.05. As revealed by previous works, both φ and ϕ are important to the electronic and magnetic properties of Sr_2IrO_4 [31,32], as evidenced hereafter.

The Ga substituting for Ir in Sr_2IrO_4 is expected to introduce holes to the system, owing to the lower valance state of Ga^{3+} than Ir^{4+}. This is confirmed by our XPS measurements with data in Fig. S3 of the Supplemental Material [29]. By fitting the XPS data with multiple valance states of Ir ions, the presence of Ir^{5+} in the doped samples is identified, and the content of Ir^{5+} is increased with increasing x. The hole doping in $Sr_2Ir_{1-x}Ga_xO_4$ single crystals is further confirmed by Hall effect measurements (See Fig. S4 in the Supplemental Material [29]). The positive slope of all Hall resistivity curves obtained at various temperatures demonstrates the p-type characteristic in the samples. Furthermore, the hole-carrier density in the sample with $x = 0.05$ is estimated to be about one order of magnitude higher than that in the nondoped sample ($x = 0$). The charge accumulation surrounding Ir ions promotes the local Coulomb repulsion, and thus suppresses the Ir-p/O-d hybridization and the structure distortion [28]. In contrast, the introduction of nonmagnetic Ga ions is expected to enhance local p-d hybridization and therefore the structure distortion because of the empty d orbit of Ga^{3+}. The two factors compete with each other and determine the structure distortion in the samples. It seems that as $x < 0.05$ the sudden enhancement of hole-carrier density in the samples lets the first factor stand out, giving rise to the enhanced Ir-O-Ir bond angle φ. Further increasing Ga content over 0.05 allows the second factor to be dominant, and as a consequence the structure distortion in the samples becomes more problematic, i.e., φ is reduced at $x > 0.05$.

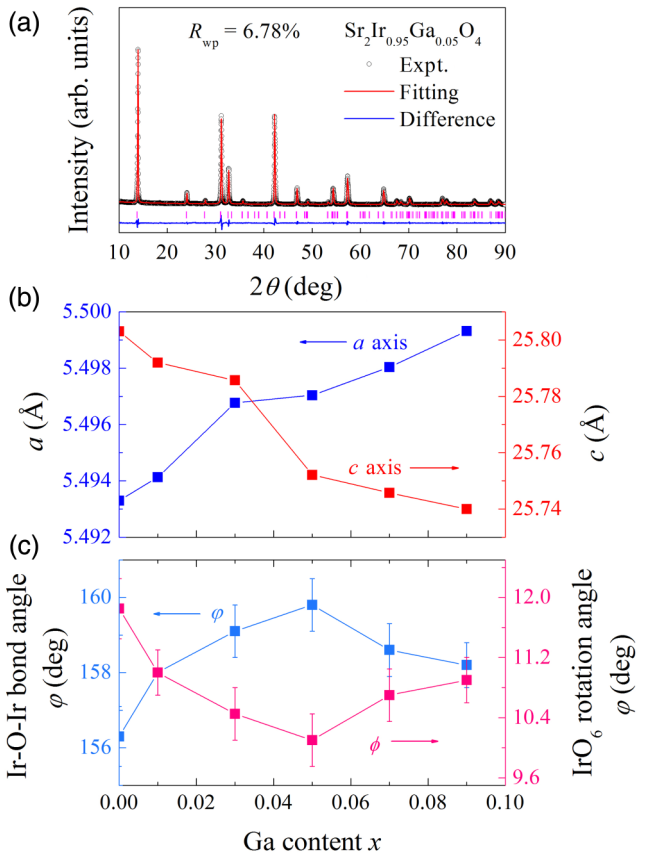

FIG. 1. (a) Rietveld refinement for the sample with $x = 0.05$. (b) Evaluated lattice parameters a and c, and (c) Ir-O-Ir bond angle φ and IrO_6 rotation angle ϕ as a function of Ga content x.

Another effect of the charge-transfer process by Ga doping is the drastic reduction in resistivity (ρ), as shown in Figs. 2(a) and 2(b), which is seen to be more than six orders of magnitude at low T. The massive variation in electric transport in $Sr_2(Ir_{1-x}Ga_x)O_4$ crystals evidences the significant effect of hole doping in tuning the $J_{eff} = 1/2$ state. As anticipated, the nondoped Sr_2IrO_4 exhibits the insulating transport in the entire T range, owing to the $J_{eff} = 1/2$ Mott state [11]. Increasing x causes the continuous suppression of $\rho(T)$ curves, and finally triggers a metallic transport in samples with higher $x \geq 0.05$, evidenced by the positive slope of $\rho(T)$ curves shown in the insets of Figs. 2(a) and 2(b). The electric transport of the c axis and the ab plane show the similar transition from insulating to metallic, although the $\rho_{ab}(T)$ and $\rho_c(T)$ curves exhibit some differences in a quantitative sense. More details of the slope change of $\rho(T)$ can be seen in Fig. S5 of the Supplemental Material [29]. It is noted that in $Sr_2(Ir_{1-x}Rh_x)O_4$, qualitatively different transport behavior between the c axis and the ab plane, i.e., $d\rho_{ab}/dT > 0$ but $d\rho_c/dT < 0$, are revealed as $0.07 < x \leq 0.24$, which may due to the vanishing magnetic state in this doping range [33]. This is different from the present situation, and we show that the AFM orders

are robust against Ga doping in $Sr_2(Ir_{1-x}Ga_x)O_4$ single crystals. Certainly, one observes the upturn in $\rho(T)$ in the low-T range (<50 K), which is due to the doping-induced disorder effect commonly seen in doped Sr_2IrO_4 [18,33].

For the tremendous modulation of electric transport and insulator-metal transition, it is critical to check whether the basal-plane AFM order remains robust against Ga doping or not. Figs. 2(c) and 2(d) show the measured magnetization data collected under $H = 0.1$ T along the [100] and [001] directions, respectively, noting the very different M axis scales for the two cases. All samples uniformly show the sharp AFM transition, and the Néel temperature T_N just presents the modest decrease from approximately 240 to approximately 180 K upon increasing x to 0.09. In particular, striking magnetic anisotropy with approximate $M_{ab}/M_c \sim 10$ can be seen for all samples. These features suggest that the basal-plane AFM configuration can be reserved for all samples, which is supported by further magnetic characterizations shown below. Magnetic and transport properties are summarized in the phase diagram plotted in Fig. 2(e), where we see the coexistence of AFM orders with different electronic states (insulator and metal).

In Sr_2IrO_4, a unique character of the basal-plane AFM order is the collective canting of Ir isospins due to the Dzyaloshinsky-Moriya (DM) interaction, which induces net magnetic moment in each IrO_2 plane [32,34,35]. As schematically shown in Fig. 3(a), within the ab plane, the AFM-ordered isospins deviate from the b axis with a certain angle α. It is revealed that the canted Ir isospins rigidly track the IrO_6 rotation ϕ relative to the c axis, leading to a locking effect of $\alpha \sim \phi$ [32]. This isospin canting leads to a net magnetic moment along the a axis with $M_a = M_{Ir}\cdot\sin\alpha \approx M_{Ir}\cdot\sin\phi$ in the IrO_2 plane [35]. In the ground state, M_a is aligned antiferromagnetically along the c axis without showing macroscopic magnetization. Upon a sufficient magnetic field H higher than the critical field H_{flip} for isospin flip within the ab plane, an isospin-flip transition is triggered, and thus a weak ferromagnetic (FM) phase arises below T_N [36,37]. This is responsible for the sudden M enhancement at T_N of the $M(T)$ curves [Figs. 2(c) and 2(d)]. The induced weak FM phase can also be identified by the well-shaped $M(H)$ curve with clear magnetic saturation, such as the one measured at $T = 10$ K in Sr_2IrO_4 shown in Fig. 3(b). A closer look at the $M(H)$ curve reveals a steplike anomaly at approximately 0.2 T, which is obviously the flipping field H_{flip}, as shown in Fig. 3(c), owing to the H-driven isospin-flop transition. The complementary initial $M(H)$ curves after the ZFC sequence are shown in Fig. S6 of the Supplemental Material [29].

Increasing x to 0.09 does not cause apparent impact onto the magnetic saturation of all the samples, while the maximum magnetization M_s derived at $H = 5$ T decreases from approximately 0.093 to approximately 0.06 μ_B/Ir, mainly ascribed to the hole-doping-induced Ir^{4+} to Ir^{5+} conversion. Another visible effect of the Ga doping is the appearance of FM-like hysteresis in samples with $x \geq 0.05$, as shown in Fig. 3(c). As revealed by previous neutron scattering experiments and theoretical calculations, hole doping in Sr_2IrO_4 is expected to reverse M_a alternatively, resembling the H-induced isospin-flop transition [38,39]. Nevertheless, the flopping of M_a driven by the hole doping is found to be irreversible, which explains the FM-like hysteresis in the samples with relatively high-doping content well. Here it is noteworthy that the basal-plane AFM orders seen in the parent material Sr_2IrO_4 are expected to be preserved in all samples, although Ga doping has modified the alignment of M_a.

As aforementioned, M_a arises from the isospin canting, and is simply determined by the canting angle α (or the octahedral rotation angle ϕ) and the Ir moment M_{Ir} with the equation $M_a = M_{Ir}\cdot\sin\alpha \approx M_{Ir}\cdot\sin\phi$. This therefore provides a quantitative measure to verify the basal-plane AFM lattice in the doped samples. In Fig. 3(d), the calculated $M_a = M_{Ir}\cdot\sin\phi$ are in good agreement with the experimental values M_s for all samples. This demonstrates the basal-plane AFM lattice exists in all samples. Here, ϕ is obtained through the structural refinement shown above, and M_{Ir} is derived from the Curie-Weiss fitting of the magnetization data (see Fig. S7 of the Supplemental Material [29]).

To this stage, we have revealed continuous tuning of the electric transport from insulating state to metallic state and robust basal-plane AFM orders in Ga-doped Sr_2IrO_4 single crystals. This is also a quite unusual and emergent phenomenon, demonstrating that the nonmagnetic substitution of Ir in Sr_2IrO_4 could be an appreciated route to accommodate the coexistence of AFM order and metallic state. Then we turn our focus to track the spintronics functionality, i.e., the AMR effect, which is the main motivation of the present work, noting that a realization of AMR represents an important step towards the manipulation and detection of AFM orders, in analogy to the traditional FM spintronics. As shown in Figs. 4(a) and 4(b), all samples with either insulating or metallic transport show the same fourfold AMR $= [R(\Phi) - R(0)]/R(0)$ symmetry, while the AMR amplitude is gradually reduced upon Ga doping. The device geometry of the AMR measurements is shown in the inset of Fig. 4(c), where the electric current is applied along the [001] direction, and H is rotated within the basal plane during the measurements. The AMR amplitude as a function of x derived at $T = 50$ and 90 K is summarized in Fig. 4(d). In Sr_2IrO_4, the AMR is found to be as huge as approximately 16.8% at $T = 50$ K, in agreement with a previous report [5]. Doping Ga at the Ir site up to $x = 0.05$ reduces the AMR amplitude from 16.8 to 1%. For samples with $x \geq 0.05$ where the metallic transport emerges, the AMR amplitude evolves with x steadily at a level of approximately 1%, which is indeed among the

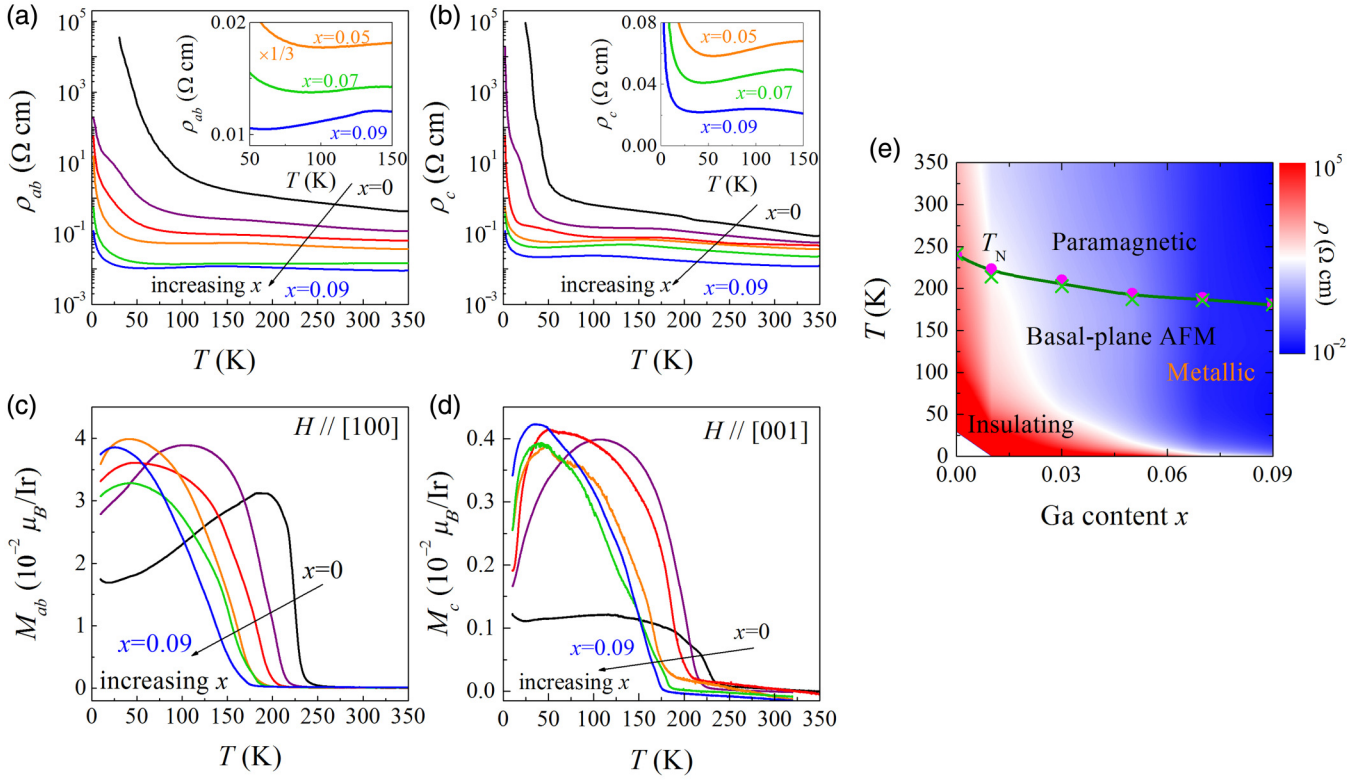

FIG. 2. Measured resistivity as a function of temperature (a) $\rho_{ab}(T)$ and (b) $\rho_c(T)$ for the samples with $x = 0$, 0.01, 0.03, 0.05, 0.07, 0.09. The inset highlights the metallic transport of the samples with $x \geq 0.05$. (c),(d) The temperature dependence of magnetization measured with $H//ab$ plane and $H//c$ axis for all samples, respectively. (e) Summarized magnetic and transport properties. The T_N were obtained from the in plane (magenta dots) and out-of-plane (green cross) magnetization data, respectively. The resistivity measurements of the *ab* plane are used to construct the phase diagram.

largest values reported so far in metallic AFM materials. The same fourfold AMR symmetry can be generally seen below T_N in all samples, while their magnitude show a gradual decrease with increasing T, as shown in Fig. 4(d).

IV. DISCUSSION

We now discuss the observed insulator-metal transition, robust basal-plane AFM orders, and persistently large fourfold AMR in $Sr_2(Ir_{1-x}Ga_x)O_4$ $(0 \leq x \leq 0.09)$ single crystals. The insulator-metal transition has been frequently observed in electron- or hole-doped Sr_2IrO_4. Regarding the electron doping in Sr_2IrO_4, the Mott gap collapses as a result of band filling, which is identified through optical spectroscopy characterizations [40]. However, the hole-doping-induced transition to metallic state is a little more complicated. First, the hole doping can move down the chemical potential to or near the top of the lower Hubbard band [41]. Second, doping with 3*d* or 4*d* species at the Ir site is expected to reduce the effective SOC; thus shrinking the bandgap in the $J_{\text{eff}} = 1/2$ state [20]. In the present work, the Ga doping at the Ir site in Sr_2IrO_4 fulfills the two factors simultaneously, i.e., introduces holes to the Ir site and reduces the effective SOC. Therefore, the downshift of chemical potential assisted by the reduction of effective SOC should be the origin of the metallic transport in $Sr_2(Ir_{1-x}Ga_x)O_4$ crystals. In addition, our structural analysis reveals a small increase (approximately 2%) of the Ir-O-Ir bond angle φ, which contributes to the conduction as well, according to density-functional calculations [31].

Previous studies revealed that the basal-plane AFM lattice of Sr_2IrO_4 is easy to break upon doping [15,18,20,21]. However, it is noted that magnetic species were generally used for the substitution in these works, which would certainly bring in additional magnetic disturbance along with the carrier doping. In a recent work, it was experimentally found that a tiny 3% of isovalent Tb^{4+} substituting for Ir^{4+} completely suppressed the long-range AFM orders in Sr_2IrO_4 [42]. Upon Mn doping in Sr_2IrO_4, the isospins were reordered from the basal plane to the *c* axis, although typical insulating transport behavior was seen simultaneously [15]. These works demonstrated the significant role of magnetic perturbation in tuning the AFM coupling in Sr_2IrO_4. According to recent theoretical calculations, the basal-plane AFM lattice behaves indeed robustly against pure carrier doping in Sr_2IrO_4 [25–27]. Therefore, it is

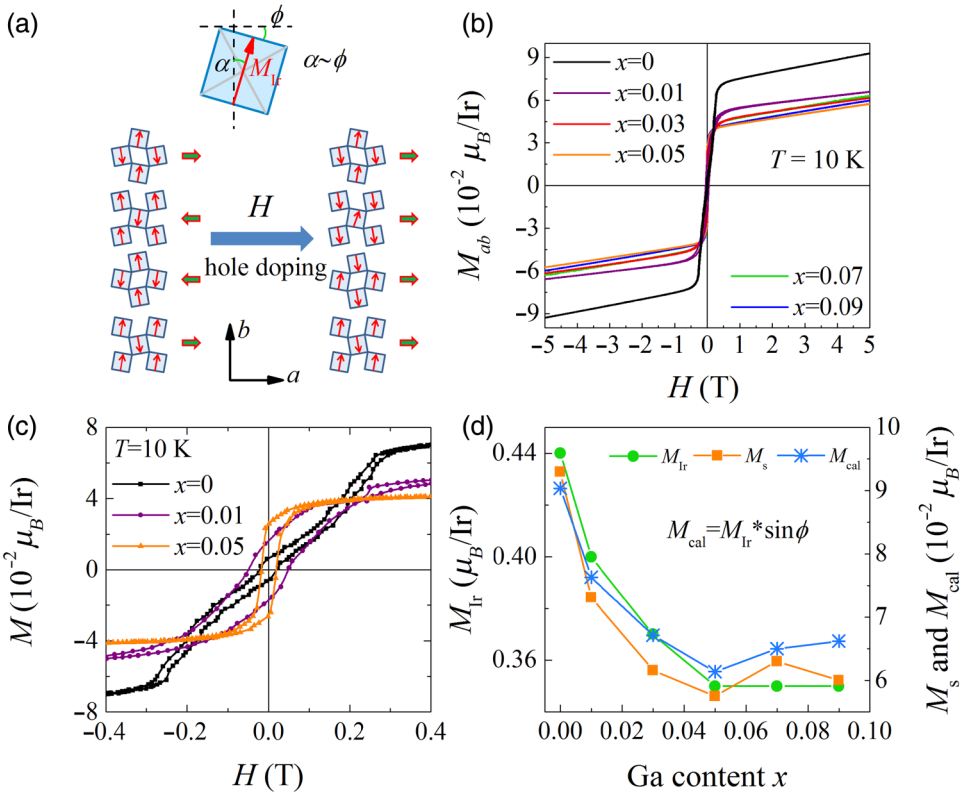

FIG. 3. (a) Sketch of the magnetic structure of Sr_2IrO_4. (b) Magnetization as a function of H measured at $T = 10$ K for all samples. (c) The $M(H)$ curves at low-field range for samples with $x = 0$, 0.01, 0.05. (d) Plotted x dependence of magnetic moment M_{Ir} obtained from Curie-Weiss fitting, M_s derived from the $M(H)$ curves, and M_{cal} calculated using the equation of $M_{cal} = M_{Ir} \cdot \sin\phi$.

physically reasonable to anticipate the preservation of the basal-plane AFM lattice in the nonmagnetic Ga-doped Sr_2IrO_4, where only the hole-carrier density is enhanced.

Our structural analysis reveals clear variation in the Ir-O-Ir bond angle φ and the octahedral rotation ϕ upon Ga doping, which may be related to the Ga-doping-induced charge transfer as discussed above. In particular, it is found that φ decreases again as $x > 0.05$, evidencing the enhancement of structure distortion in the samples. This is expected to stabilize the AFM orders. As shown in Fig. S8 of the Supplemental Material [29], T_N evolves with x in a more modest manner at $x > 0.05$ indeed, as compared with the case at $x < 0.05$. This is consistent with the structural analysis. In addition, topological defects accompanying with the Ga doping will surely impact the Ir AFM network and thus contribute to the continuous decrease in

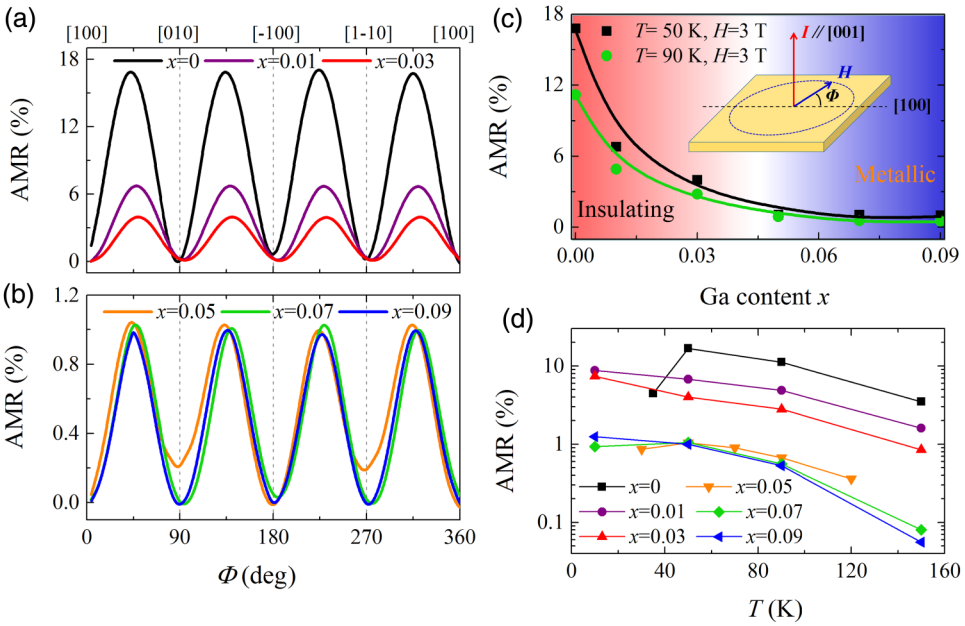

FIG. 4. (a),(b) Measured AMR data at $T = 50$ K and $H = 3$ T for all samples. (c) AMR magnitude obtained at $T = 50$ K (black squares) and 90 K (green dots) as a function of Ga content x. The inset shows the device geometry of the AMR measurements. (d) Temperature dependence of AMR magnitude for all samples.

T_N within the entire doping range. We note that a similar transition from insulating to metallic was reported in polycrystalline $Sr_{2-x}Ga_xIrO_4$ recently [43]. However, this Ga replacement of Sr gives rise to the electron-doping effect in the samples, and rather complicated magnetic states were revealed in this work, different from our results.

The key experimental observation of the present work is the large fourfold AMR effect in all samples hosting remarkably different transport properties. This has not been reported in previous studies focusing on the AFM spintronics. The realization of the AFM AMR effect is crucial for the manipulation and detection of AFM orders. The above magnetization data reveal that the weak FM phase can be induced by either magnetic field or hole doping. This provides a natural handle to manipulate the basal-plane AFM orders, and thus trigger the AMR effect in the samples. During the AMR measurements, H and thereby M is always perpendicular to the applied electric current, which means that the AMR is determined solely by the varying angle between M and crystal axes, fulfilling the scheme of magnetocrystalline anisotropy. Previous neutron scattering and optical microscopy characterizations have demonstrated that the magnetic easy axis of Sr_2IrO_4 is along the crystal axis, i.e., the b axis [32,35]. This should be the same case in all doped samples, since they have the same basal-plane AFM configuration as evidenced by our magnetic characterizations. As shown in Figs. 4(a) and 4(b), the AMR minima of all samples has a periodicity of $\pi/2$, and appears right at the crystal axes, matching well with the tetragonal symmetry of the crystals. This clearly demonstrates the magnetocrystalline anisotropy origin of the observed persistent large AMR in all samples.

It is known that the crystalline AMR is determined by the anisotropy of the DOS and the corresponding position of the chemical potential. In the present work, the Ga doping is revealed to modify the $J_{\text{eff}} = 1/2$ state significantly. Therefore, the observation of different AMR magnitudes in the samples with different Ga content is expected. Moreover, it was theoretically revealed that the DOS anisotropy of the AFM insulator Sr_2IrO_4 is far larger than that of AFM metals, i.e., MnIr and Mn_2Au [3,10]. This indicates that the AFM insulators are better for obtaining a sizable AMR effect, as compared with the AFM metals. In Figs. 4(c) and 4(d), the AMR magnitude of the samples showing insulating transport ($x < 0.05$) is much larger overall than that of the samples with $x \geq 0.05$, where metallic transport appears, which is in agreement with the theoretical revealing [3,10].

V. CONCLUSION

To conclude, we report the observation of persistent large AMR effects and insulator-metal transition in the $J_{\text{eff}} = 1/2$ antiferromagnets $Sr_2(Ir_{1-x}Ga_x)O_4$ ($0 \leq x \leq 0.09$). Our results reveal that the Ga doping to the $J_{\text{eff}} = 1/2$ Mott state in Sr_2IrO_4 can continuously suppress the insulating transport, and eventually lead to a metallic behavior. Meanwhile, the basal-plane AFM orders exhibit robustness against the Ga doping and exists in all samples well. Importantly, the fourfold AMR is generally evidenced in all samples with remarkably different transport properties, which can be understood as a consequence of magnetocrystalline anisotropy. It is noted that the AMR in these samples with metallic transport can still be as large as approximately 1%, which is yet among the largest values reported in AFM metals. These findings suggest that the spin-orbit-coupled antiferromagnets $Sr_2(Ir_{1-x}Ga_x)O_4$ are favorable candidates for exploiting emergent phenomena and functionalities within the concept of AFM spintroncis.

ACKNOWLEDGMENTS

This work is supported by the National Nature Science Foundation of China (Grant Nos. 11774106, 11674055, 51721001, and 51431006), the National Key Research Projects of China (Grant No. 2016YFA0300101).

[1] B. G. Park, J. Wunderlich, X. Marti, V. Holy, Y. Kurosaki, M. Yamada, H. Yamamoto, A. Nishide, J. Hayakawa, H. Takahashi, A. B. Shick, and T. Jungwirth, A spin-valve-like magnetoresistance of an antiferromagnet-based tunnel junction, Nat. Mater. **10**, 347 (2011).

[2] V. M. Barthem, C. V. Colin, H. Mayaffre, M. H. Julien, and D. Givord, Revealing the properties of Mn_2Au for antiferromagnetic spintronics, Nat. Commun. **4**, 2892 (2013).

[3] I. Fina, X. Marti, D. Yi, J. Liu, J. H. Chu, C. Rayan-Serrao, S. Suresha, A. B. Shick, J. Zelezny, T. Jungwirth, J. Fontcuberta, and R. Ramesh, Anisotropic magnetoresistance in an antiferromagnetic semiconductor, Nat. Commun. **5**, 4671 (2014).

[4] X. Marti, I. Fina, C. Frontera, J. Liu, P. Wadley, Q. He, R. J. Paull, J. D. Clarkson, J. Kudrnovsky, I. Turek, J. Kunes, D. Yi, J. H. Chu, C. T. Nelson, L. You, E. Arenholz, S. Salahuddin, J. Fontcuberta, T. Jungwirth, and R. Ramesh, Room-temperature antiferromagnetic memory resistor, Nat. Mater. **13**, 367 (2014).

[5] C. Wang, H. Seinige, G. Cao, J. S. Zhou, J. B. Goodenough, and M. Tsoi, Anisotropic Magnetoresistance in Antiferromagnetic Sr_2IrO_4, Phys. Rev. X **4**, 041034 (2014).

[6] R. Galceran, I. Fina, J. Cisneros-Fernandez, B. Bozzo, C. Frontera, L. Lopez-Mir, H. Deniz, K. W. Park, B. G. Park, L. Balcells, X. Marti, T. Jungwirth, and B. Martinez, Isothermal anisotropic magnetoresistance in antiferromagnetic metallic IrMn, Sci. Rep. **6**, 35471 (2016).

[7] T. Jungwirth, X. Marti, P. Wadley, and J. Wunderlich, Antiferromagnetic spintronics, Nat. Nanotechnol. **11**, 231 (2016).

[8] P. Wadley, B. Howells, J. Zelezny, C. Andrews, V. Hills, R. P. Campion, V. Novak, K. Olejnik, F. Maccherozzi, S. S. Dhesi, S. Y. Martin, T. Wagner, J. Wunderlich, F. Freimuth,

Y. Mokrousov, J. Kunes, J. S. Chauhan, M. J. Grzybowski, A. W. Rushforth, K. W. Edmonds, B. L. Gallagher, and T. Jungwirth, Electrical switching of an antiferromagnet, Science **351**, 587 (2016).

[9] C. L. Lu, B. Gao, H. W. Wang, W. Wang, S. L. Yuan, S. Dong, and J. -M. Liu, Revealing controllable anisotropic magnetoresistance in spin-orbit coupled antiferromagnet Sr_2IrO_4, Adv. Funct. Mater. **28**, 1706589 (2018).

[10] A. B. Shick, S. Khmelevskyi, O. N. Mryasov, J. Wunderlich, and T. Jungwirth, Spin-orbit coupling induced anisotropy effects in bimetallic antiferromagnets: A route towards antiferromagnetic spintronics, Phys. Rev. B **81**, 212409 (2010).

[11] B. J. Kim, H. Jin, S. J. Moon, J. Y. Kim, B. G. Park, C. S. Leem, J. Yu, T. W. Noh, C. Kim, S. J. Oh, J. H. Park, V. Durairaj, G. Cao, and E. Rotenberg, Novel $J_{\rm eff}$=1/2 Mott State Induced by Relativistic Spin-Orbit Coupling in Sr_2IrO_4, Phys. Rev. Lett. **101**, 076402 (2008).

[12] Y. S. Hou, H. J. Xiang, and X. G. Gong, Unveiling the origin of the basal-plane antiferromagnetism in the spin–orbit Mott insulator Ba_2IrO_4: A density functional and model Hamiltonian study, New J. Phys. **18**, 043007 (2016).

[13] H. Zhang, K. Haule, and D. Vanderbilt, Effective J=1/2 Insulating State in Ruddlesden-Popper Iridates: An LDA+DMFT Study, Phys. Rev. Lett. **111**, 246402 (2013).

[14] S. Fujiyama, K. Ohashi, H. Ohsumi, K. Sugimoto, T. Takayama, T. Komesu, M. Takata, T. Arima, and H. Takagi, Weak antiferromagnetism of $J_{\rm eff}$=1/2 band in bilayer iridate $Sr_3Ir_2O_7$, Phys. Rev. B **86**, 174414 (2012).

[15] S. Calder, G. X. Cao, S. Okamoto, J. W. Kim, V. R. Cooper, Z. Gai, B. C. Sales, M. D. Lumsden, D. Mandrus, and A. D. Christianson, $J_{\rm eff}$=1/2 Mott spin-orbit insulating state close to the cubic limit in Ca_4IrO_6, Phys. Rev. B **89**, 081104 (2014).

[16] A. P. Mackenzie, T. Scaffidi, C. W. Hicks, and Y. Maeno, Even odder after twenty-three years: The superconducting order parameter puzzle of Sr_2RuO_4, npj Quant. Mater. **2**, 40 (2017).

[17] L. Xu, N. A. Bogdanov, A. Princep, P. Fulde, J. van den Brink, and L. Hozoi, Covalency and vibronic couplings make a nonmagnetic j =3/2 ion magnetic, npj Quant. Mater. **1**, 16029 (2016).

[18] X. Chen, T. Hogan, D. Walkup, W. Zhou, M. Pokharel, M. Yao, W. Tian, T. Z. Ward, Y. Zhao, D. Parshall, C. Opeil, J. W. Lynn, V. Madhavan, and S. D. Wilson, Influence of electron doping on the ground state of $(Sr_{1-x}La_x)_2IrO_4$, Phys. Rev. B **92**, 075125 (2015).

[19] M. Ge, T. F. Qi, O. B. Korneta, D. E. De Long, P. Schlottmann, W. P. Crummett, and G. Cao, Lattice-driven magnetoresistivity and metal-insulator transition in single-layered iridates, Phys. Rev. B **84**, 100402 (2011).

[20] J. P. Clancy, A. Lupascu, H. Gretarsson, Z. Islam, Y. F. Hu, D. Casa, C. S. Nelson, S. C. LaMarra, G. Cao, and Y.-J. Kim, Dilute magnetism and spin-orbital percolation effects in $Sr_2Ir_{1-x}Rh_xO_4$, Phys. Rev. B **89**, 054409 (2014).

[21] S. J. Yuan, S. Aswartham, J. Terzic, H. Zheng, H. D. Zhao, P. Schlottmann, and G. Cao, From $J_{\rm eff}$=1/2 insulator top-wave superconductor in single-crystal $Sr_2Ir_{1-x}Ru_xO_4$ ($0\leq x\leq 1$), Phys. Rev. B **92**, 245103 (2015).

[22] Y. K. Kim, O. Krupin, J. D. Denlinger, A. Bostwick, E. Rotenberg, Q. Zhao, J. F. Mitchell, J. W. Allen, and B. J. Kim, Fermi arcs in a doped pseudospin-1/2 Heisenberg antiferromagnet, Science **345**, 187 (2014).

[23] I. Battisti, K. M. Bastiaans, V. Fedoseev, A. de la Torre, N. Iliopoulos, A. Tamai, E. C. Hunter, R. S. Perry, J. Zaanen, F. Baumberger, and M. P. Allan, Universality of pseudogap and emergent order in lightly doped Mott insulators, Nat. Phys. **13**, 21 (2016).

[24] Y. K. Kim, N. H. Sung, J. D. Denlinger, and B. J. Kim, Observation of a d-wave gap in electron-doped Sr_2IrO_4, Nat. Phys. **12**, 37 (2015).

[25] H. Watanabe, T. Shirakawa, and S. Yunoki, Monte Carlo Study of an Unconventional Superconducting Phase in Iridium Oxide $J_{\rm eff}$=1/2 Mott Insulators Induced by Carrier Doping, Phys. Rev. Lett. **110**, 027002 (2013).

[26] Z. Y. Meng, Y. B. Kim, and H. Y. Kee, Odd-Parity Triplet Superconducting Phase in Multiorbital Materials with a Strong Spin-Orbit Coupling: Application to Doped Sr_2IrO_4, Phys. Rev. Lett. **113**, 177003 (2014).

[27] S. Sumita, T. Nomoto, and Y. Yanase, Multipole Superconductivity in Nonsymmorphic Sr_2IrO_4, Phys. Rev. Lett. **119**, 027001 (2017).

[28] P. Liu, M. Reticcioli, B. Kim, A. Continenza, G. Kresse, D. D. Sarma, X.-Q. Chen, and C. Franchini, Electron and hole doping in the relativistic Mott insulator Sr_2IrO_4: A first-principles study using band unfolding technique, Phys. Rev. B **94**, 195145 (2016).

[29] See Supplemental Material at http://link.aps.org/supplemental/10.1103/PhysRevApplied.10.014025 for structural analysis, x-ray photoemission spectroscopy characterizations, and more magnetic and transport data.

[30] R. D. Shannon, Revised effective ionic radii and systematic studies of interatomic distances in halides and chalcogenides, Acta Crystallogr. A **32**, 751 (1976).

[31] S. J. Moon, H. Jin, W. S. Choi, J. S. Lee, S. S. A. Seo, J. Yu, G. Cao, T. W. Noh, and Y. S. Lee, Temperature dependence of the electronic structure of the $J_{\rm eff}$=1/2 Mott insulator Sr_2IrO_4 studied by optical spectroscopy, Phys. Rev. B **80**, 195110 (2009).

[32] S. Boseggia, H. C. Walker, J. Vale, R. Springell, Z. Feng, R. S. Perry, M. Moretti Sala, H. M. Ronnow, S. P. Collins, and D. F. McMorrow, Locking of iridium magnetic moments to the correlated rotation of oxygen octahedra in Sr_2IrO_4 revealed by x-ray resonant scattering, J. Phys.: Condens. Matter **25**, 422202 (2013).

[33] T. F. Qi, O. B. Korneta, L. Li, K. Butrouna, V. S. Cao, X. Wan, P. Schlottmann, R. K. Kaul, and G. Cao, Spin-orbit tuned metal-insulator transitions in single-crystal $Sr_2Ir_{1-x}Rh_xO_4$ ($0\leq x\leq 1$), Phys. Rev. B **86**, 125105 (2012).

[34] G. Jackeli and G. Khaliullin, Mott Insulators in the Strong Spin-Orbit Coupling Limit: From Heisenberg to a Quantum Compass and Kitaev Models, Phys. Rev. Lett. **102**, 017205 (2009).

[35] F. Ye, S. Chi, B. C. Chakoumakos, J. A. Fernandez-Baca, T. Qi, and G. Cao, Magnetic and crystal structures of Sr_2IrO_4: A neutron diffraction study, Phys. Rev. B **87**, 140406 (2013).

[36] B. J. Kim, H. Ohsumi, T. Komesu, S. Sakai, T. Morita, H. Takagi, and T. Arima, Phase-sensitive observation of

a spin-orbital Mott state in Sr_2IrO_4, Science **323**, 1329 (2009).

[37] C. L. Lu, S. Dong, A. Quindeau, D. Preziosi, N. Hu, and M. Alexe, Dual gate control of bulk transport and magnetism in the spin-orbit insulator Sr_2IrO_4, Phys. Rev. B **91**, 104401 (2015).

[38] P. Liu, S. Khmelevskyi, B. Kim, M. Marsman, D. Li, X.-Q. Chen, D. D. Sarma, G. Kresse, and C. Franchini, Anisotropic magnetic couplings and structure-driven canted to collinear transitions in Sr_2IrO_4 by magnetically constrained noncollinear DFT, Phys. Rev. B **92**, 054428 (2015).

[39] F. Ye, X. Wang, C. Hoffmann, J. Wang, S. Chi, M. Matsuda, B. C. Chakoumakos, J. A. Fernandez-Baca, and G. Cao, Structure symmetry determination and magnetic evolution in $Sr_2Ir_{1-x}Rh_xO_4$, Phys. Rev. B **92**, 201112 (2015).

[40] A. de la Torre, S. McKeown Walker, F. Y. Bruno, S. Ricco, Z. Wang, I. Gutierrez Lezama, G. Scheerer, G. Giriat, D. Jaccard, C. Berthod, T. K. Kim, M. Hoesch, E. C. Hunter, R. S. Perry, A. Tamai, and F. Baumberger, Collapse of the Mott Gap and Emergence of a Nodal Liquid in Lightly Doped Sr_2IrO_4, Phys. Rev. Lett. **115**, 176402 (2015).

[41] Y. Cao, Q. Wang, J. A. Waugh, T. J. Reber, H. Li, X. Zhou, S. Parham, S. R. Park, N. C. Plumb, E. Rotenberg, A. Bostwick, J. D. Denlinger, T. Qi, M. A. Hermele, G. Cao, and D. S. Dessau, Hallmarks of the Mott-metal crossover in the hole-doped pseudospin-1/2 Mott insulator Sr_2IrO_4, Nat. Commun. **7**, 11367 (2016).

[42] J. C. Wang, S. Aswartham, F. Ye, J. Terzic, H. Zheng, D. Haskel, S. Chikara, Y. Choi, P. Schlottmann, R. Custelcean, S. J. Yuan, and G. Cao, Decoupling of the antiferromagnetic and insulating states in Tb-doped Sr_2IrO_4, Phys. Rev. B **92**, 214411 (2015).

[43] T. Han, Y. J. Wang, J. Yang, L. He, J. M. Xu, D. D. Liang, H. Han, M. Ge, C. Y. Xi, W. K. Zhu, C. J. Zhang, and Y. H. Zhang, Enhanced electrical conductivity and diluted Ir^{4+} spin orders in electron doped iridates $Sr_{2-x}Ga_xIrO_4$, Appl. Phys. Lett. **109**, 192409 (2016).